RESEARCH ARTICLE

Check for updates

Copper-incorporation for polytypism and bandgap engineering of MAPbBr₃ perovskite thin films with enhanced near-Infrared photocurrent-response†

Amr Elattar, [iD] *[ab] Jiban Kangsabanik,[c] Kodai Nakao,[a] Kosei Tsutsumi,[a] Hiroo Suzuki,[a] Takeshi Nishikawa,[a] Kristian S. Thygesen[c] and Yasuhiko Hayashi [iD] [a]

The optoelectronic properties of lead-based halide perovskites can be enhanced through B-site engineering. Here, we studied the B-site alloying of MAPbBr₃ thin films with copper (Cu^{2+}). The alloyed perovskite thin films were characterized by a dark color, enlarged average grain boundary, and lowering of the optical bandgap from 2.32 eV for pristine MAPbBr₃ to 1.85 eV for 50% Cu-substituted MAPbBr₃. Various characterization methods revealed that the Cu-incorporation leads to the appearance of a Cu-rich secondary phase. The conductivity increased over three orders of magnitude upon alloying. Temperature-dependent conductivity measurements at temperatures ranging from 110 K to 300 K revealed the occurrence of two phase-transitions in Cu-substituted perovskite, and only one transition in pristine MAPbBr₃. Photocurrent measurements of the alloyed perovskites showed that band-carrier generation occurred upon excitation in the near-infrared region. First-principles point defect calculation shows the likelihood of compensating Br vacancy formation with high Cu-substituting concentrations. Calculation of atomic orbital projected density of states ($Cu_{Pb} + v_{Br}$ defect complex) revealed the presence of localized defect states within the pristine bandgap, explaining the observed sub-bandgap absorption. The results provide an insight into the alloying importance in phase-modulation and tailoring the optoelectronic properties of perovskites for a wide range of efficient optoelectronic devices.

Introduction

Lead-based perovskites have been widely utilized in optoelectronic devices, owing to their attractive features of strong absorption coefficient,[1–3] high charge carrier mobility,[4–8] tunable bandgap,[9–12] long diffusion length,[13–15] and low exciton binding energies.[16–19] One of the fundamental approaches to developing efficient perovskite-based optoelectronic devices is doping/alloying. *Via* doping, defect/impurity levels, introduced by dopants, overlap with the valence band (or the conduction band) of the host perovskite. As a result, different perovskites with versatile optical and electrical properties can be manipulated. Three types of MAPbX₃ doping have (in general) been investigated in

numerous studies: (1) A-site doping where a methylammonium MA^+ cation is doped with A^+ (A^+ = FA^+, Rb^+, Cs^+, or K^+).[20–30] (2) B-site doping where lead Pb^{2+} is doped with different metal cations M^{n+} (M^{n+} = Sn^{2+}, Ca^{2+}, Cd^{2+}, Sr^{2+}, Bi^{3+}, Au^{3+}, Ba^{2+}, Mn^{2+}, Ni^{2+}, In^{3+}, Cu^{2+}, or Er^{3+}).[31–44] (3) Halide anion X^- doping with different anions (Cl^-, Br^-, I^-, or Se^{2-}).[45–49]

MAPbBr₃ perovskite has considerable potential for laser applications[50–53] and photodetection.[54,55] Various investigations have focused on enhancing the optoelectronic properties of this material *via* doping. Deng *et al.* have studied NH_4^+-doped MAPbBr₃ perovskite quantum dots.[56] They found that NH_4^+ inhibits non-radiative recombinations and reduces the defect density of MAPbBr₃. Li *et al.* have proposed local lattice strain compensation of Zn^{2+}-doped MAPbBr₃ single crystal for photo-restriction under light illumination.[57] Furthermore, through Er^{3+}-doping, the responsivity and external quantum efficiency of MAPbBr₃ single crystal photodetector increased five-fold relative to that of the pristine crystal.[44] Moreover, Bi^{3+}-doped MAPbBr₃ single crystals have been extensively investigated. Early investigations by Abdelhady *et al.* suggested that Bi-doping-induced changes in the absorption spectrum resulted from bandgap modulation.[39] However, subsequent studies showed

a Graduate School of Natural Science and Technology, Okayama University, 3-1-1 Tsushimanaka, Kita-ku, Okayama 700-8530, Japan. E-mail: psgx8nrx@s.okayama-u.ac.jp

b Department of Chemistry, Faculty of Science, Ain Shams University, 11566 Cairo, Egypt

c CAMD, Department of Physics, Technical University of Denmark, 2800 Kongens Lyngby, Denmark

that Bi-doping increases the trap states within the bandgap of the MAPbBr$_3$ host without any effect on the bandgap and the exciton binding energy.[38,40,42,43,58]

Polytypism is one example of polymorphism where the crystal structure is identical along two dimensions but different along the third dimension. Polytypism of hybrid lead-based perovskites has been reported in a few papers.[59–61] The polytypes of hybrid perovskite structure ABX$_3$ depend on the stacking sequence of the close-packed AX$_3$ layers. The most common polytype of hybrid perovskite is the 3C polytype with BX$_6$ corner-sharing octahedra, which is favorable for perovskites with tolerance factors of $t \leq 1$.[60] The label of 3C resembles the three close-packed layers of the aristotype cubic cell (C).[62] The other most common polytypes of perovskite oxides are hexagonal polytypes, which are favorable for perovskites with tolerance factors of $t > 1$, which can be obtained through using large A-cations or small B-cations.[61] A 2H hexagonal polytype with BX$_6$ face-sharing octahedra leads to a one-dimensional (1D) array.[59] However, the other 4H and 6H hexagonal polytypes, which have three-dimensional (3D) frameworks, are composed of BX$_6$ face-sharing octahedra (h) and BX$_6$ corner-sharing octahedra (C).[60]

In this study, we have investigated the Cu^{2+}-chemical alloying effect on MAPbBr$_3$ as a host material. Upon substitution, MA(Pb:Cu)Br$_3$, thin films exhibit color darkness with increasing size of the average grain boundaries. Optical measurements indicate a sharp bandgap reduction with 50% replacement. X-ray diffraction (XRD), X-ray photoelectron spectroscopy (XPS) and energy dispersive spectroscopy (EDS) mapping measurements indicate that Cu^{2+} ions are incorporated into the MAPbBr$_3$ crystal structure with the appearance of a new phase related

neither to the crystal structure peaks of MAPbBr$_3$ nor the initial precursor. Theoretical simulations were utilized to further explore the Cu-incorporation mechanism. Photocurrent measurements of the doped perovskites revealed band carrier generation at an excitation photon energy below the bandgap, suggesting considerable potential for a wide range of optoelectronic applications.

Results and discussion

Anti-solvent assisted crystallization of methylammonium lead bromide perovskites plays the most significant role in DMF, at the crystallization temperature (70 °C).[39] In this work, pristine and Cu-alloyed MACu$_x$Pb$_{(1-x)}$Br$_3$ (where x = 0%, 10%, 20%, 30%, 40%, and 50%) polycrystalline thin films were prepared via spin-coating of the precursor solution over a glass substrate with the assistance of toluene as an anti-solvent, as shown in Fig. 1 The perovskite films with different Cu^{2+} concentrations differ in color (see Fig. 1b) from yellowish orange for the non-alloyed MAPbBr$_3$ to almost dark brown for the 50% Cu-substituted MAPbBr$_3$.

The top-view scanning electron microscopy (SEM) images presented in Fig. 2a–f show the morphology of the perovskite thin films. Upon Cu^{2+} alloying, the average grain boundary area increases from 0.042 μm^2 for pristine MAPbBr$_3$ to 0.71 μm^2 for 40% Cu-substituted MAPbBr$_3$, as shown in Fig. S1 (ESI†). However, an SEM image of the 50% Cu-substituted MAPbBr$_3$ thin film revealed that large micro-rods are formed as a side product. Energy dispersive scanning (EDS) elemental mapping
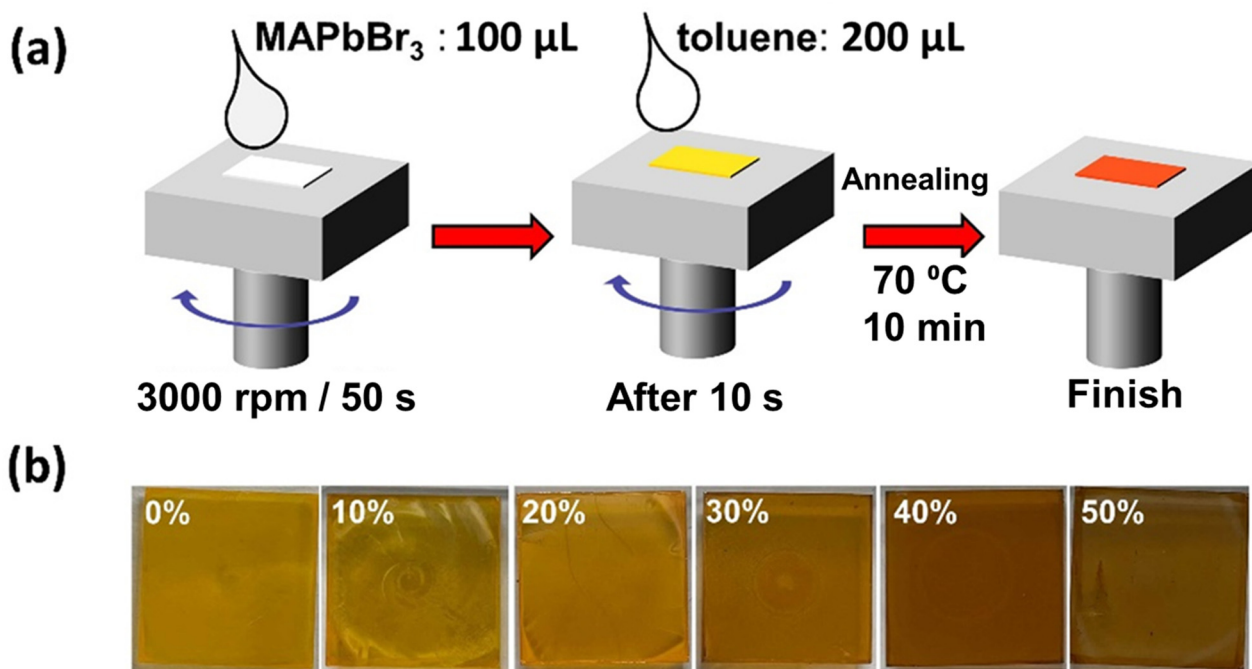

Fig. 1 (a) Graphical illustration of perovskite thin film fabrication via spin-coating. (b) Picture of pristine (0%) and (10, 20, 30, 40, and 50%) Cu-substituted MAPbBr$_3$ thin films obtained from use of (0, 10, 20, 30, 40, and 50%) [CuBr$_2$]/([CuBr$_2$] + [PbBr$_2$]) mole percentages.
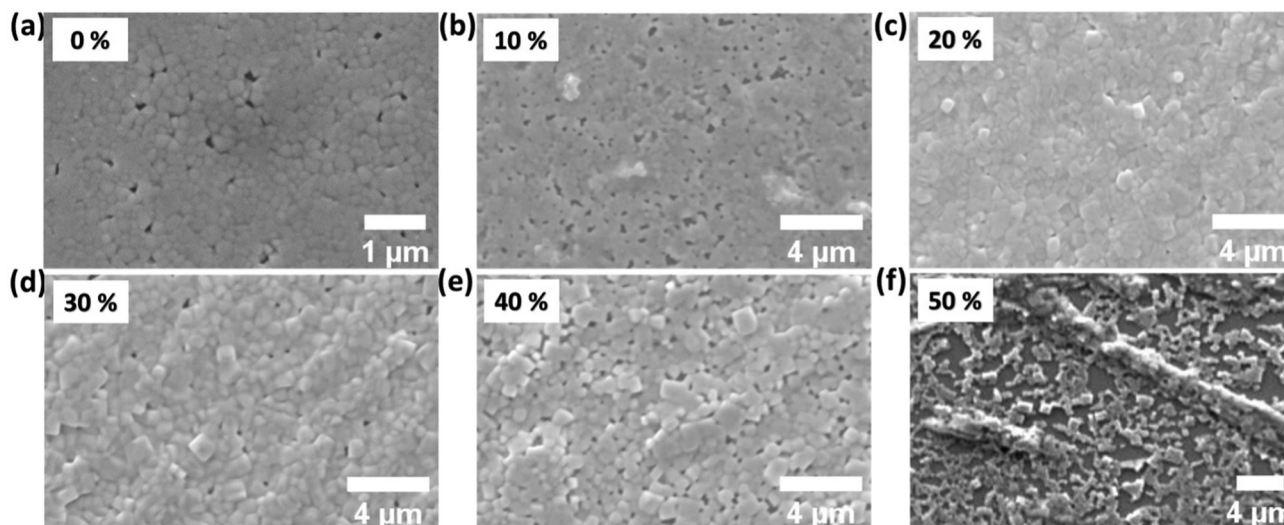
Fig. 2 SEM images of undoped (a), 10% (b), 20% (c), 30% (d), 40% (e), and 50% (f) Cu-alloyed MAPbBr$_3$ thin films.

results reveal the presence of homogeneously distributed Pb (blue-colored images in Fig. S2, ESI†). However, the Cu-

elemental mapping results (red-colored images in Fig. S2, ESI†) show the gradual increase in Cu alloying. Cu is homogeneously
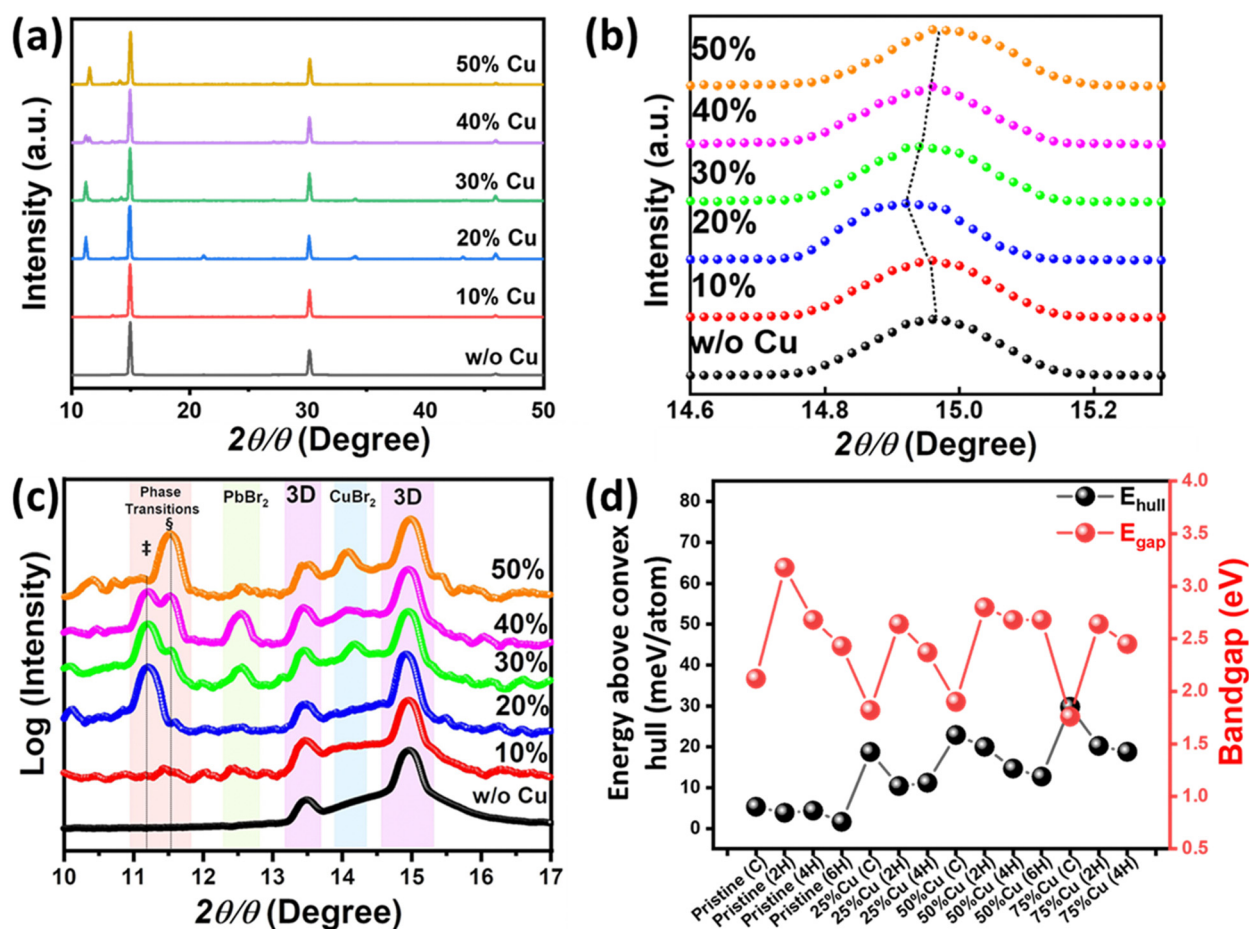

Fig. 3 (a) XRD patterns of Cu-alloyed MAPbBr$_3$ perovskite thin films. (b) XRD peak ⟨100⟩ shift upon copper addition. (c) XRD patterns (log scale) for 2θ = 10−17°. (d) Energy above convex hull and bandgap for different phases of pure and Cu-alloyed MAPbBr$_3$ where C, 2H, 4H, and 6H represent cubic, hexagonal-2H, hexagonal-4H, and hexagonal-6H phases of MAPbBr$_3$, respectively.

This journal is © The Royal Society of Chemistry and the Chinese Chemical Society 2022

distributed until an alloying level of 20% is reached. After that, a Cu-rich new phase appears in the film which is clearly observed at an alloying level of 50%.

Fig. 3a shows the XRD pattern of the pristine and Cu-substituted $MAPbBr_3$ thin films. The alloyed samples maintain the cubic perovskite structure of $MAPbBr_3$ with three main diffraction peaks at (100), (200), and (300).[63] However, with incorporation of Cu into the material, new XRD peaks occur at $2\theta = 11.2°$ (‡) and $2\theta = 11.5°$ (§). Regarding to XRD data within 2theta range $14.6°–15.3°$ (As depicted in Fig. 3b), the main diffraction peak (100) of $MAPbBr_3$ cubic structure is shifted towards lower theta with increasing of copper alloying from pristine $MAPbBr_3$ into 20% alloyed one. This reveals $MAPbBr_3$ crystal lattice expansion owing to the copper occupation of the interstitial positions through $MAPbBr_3$ cubic structure rather than Cu/Pb metal substitution. This is consistent with the large difference in effective ionic radius of Pb^{2+} (119 pm) and Cu^{2+} (73 pm). In addition, Cu perovskites show Jahn–Teller distortion which stereochemically hinders the upkeeping of 3D perovskite structure. With further Cu-alloying, the XRD peak is shifted-back to its original position. This might be accounted for the preference of Cu-atoms to form the Cu-rich secondary phases rather than the occupation of the $MAPbBr_3$ interstitial positions. A plot of the logarithm (intensity) vs. 2θ, as shown in Fig. 3c, reveals four regions. These include the purple regions of 3D-$MAPbBr_3$ and peaks corresponding to crystalline residual metal halide salt in the perovskites with Cu-concentration ranging from 30% to 50% (blue and green regions represent $CuBr_2$ and $PbBr_2$, respectively). Interestingly, the orange region reveals a new diffraction peak, which occurs for 20% Cu-substituted $MAPbBr_3$ (‡). With further substitution, the intensity of this peak decreases while the intensity of another peak (occurring at a higher angle) increases (§). These extra XRD peaks may have resulted from two factors. One factor is that the formation of Pb-substituted 2D Cu-based perovskite secondary phase MA_2CuBr_4 may have contributed to their emergence. However, this factor can be excluded as the main peak of MA_2CuBr_4 perovskite should be appeared near $2\theta = 9.2°$ not in the range ($11°–12°$) whatever the concentration of lead alloyed, as depicted in Fig. S3 (ESI†).[64] The other possible factor is the formation of a Pb-based perovskite secondary phase, owing to Cu-alloying. According to literature,[60] Pb-based perovskite, namely $(FAPbI_3)_x(MAPbBr_3)_{1-x}$, exhibits a sequential hexagonal polytypism (i.e., 2H (delta phase)-4H-6H-3R(3C)) during the crystallization process of its perovskite thin film (H, R, and C represent hexagonal, rhombohedral, and cubic phases, respectively). Moreover, the hexagonal phases have one dimensionality (1D) structure with XRD fingerprint peaks for 2θ ranging from $11.6°$ to $14.1°$, and therefore we hypothesize that both peaks, i.e., ‡ and §, correspond to new phases, which are neither related to the crystal structure of 3D-$MAPbBr_3$ nor the initial precursors. These peaks may, however, be related to 1D hexagonal polytypes of Cu-$MAPbBr_3$ perovskite, which would be consistent with the formation of a rod-shaped phase in the 50% Cu-substituted thin film. Regarding to these observations, we speculate that hexagonal polytypes of Cu-substituted $MAPbBr_3$ perovskite. This might be attributed to

the presence of $MAPbBr_3$ cubic perovskite which induces the excess copper to form polytypes of the most stable 1D microrods rather than 2D sheets.

To verify the validity of the assumption that hexagonal polytypes are formed in Cu-substituted $MAPbBr_3$, we calculated the energy above the convex hull (E_{hull}) of different phases (namely Cubic, 2H, 4H, and 6H (only for 50% alloying)) with varying substituted concentrations ($MACu_xPb_{1-x}Br_3$; $x = 0$, 0.25, 0.5, and 0.75). The possible crystal structures are presented in Fig. S4–S7 (ESI†). Fig. 3d shows E_{hull} calculation results where all possible secondary phases are taken from the Open Quantum Materials Database (OQMD).[65] E_{hull} can be seen as a measure of comparative stability between different phases. It should be noted that E_{hull} is calculated at $T = 0$ K and a finite temperature might have some effect on comparative stability. For the pristine $MAPbBr_3$ perovskite, almost the same E_{hull} is obtained for the aforementioned four phases. However, for the Cu-alloyed compounds, the E_{hull} of the hexagonal phases differs modestly (by ~10 meV per atom) from that of the cubic phase. This might explain some secondary hexagonal phase formation with Cu alloying as observed experimentally. Furthermore, the bandgap differs among the phases of the Cu-alloyed perovskites with the cubic phase showing the lowest bandgap in all the alloying concentrations. For the hexagonal phase bandgap decreases when we go from 2H > 4H > 6H.

In order to study the effect of Cu^{2+} incorporation on the elemental composition of Cu-$MAPbBr_3$ films, X-ray photoelectron spectroscopy (XPS) was performed, as depicted in Fig. 4 and Fig. S8 (ESI†). The Pb 4f spectrum for the $MAPbBr_3$ film reveals $4f_{5/2}$ and $4f_{7/2}$ peaks at 143.4 and 138.6 eV, respectively, corresponding to the Pb^{2+} cations[66] (Fig. 4a). The Br 3d spectrum (Fig. 4b) shows $3d_{3/2}$ and $3d_{5/2}$ peaks at 69.7 and 68.5 eV, respectively, corresponding to the Br^- anions. The C 1s spectrum for the $MAPbBr_3$ film presents C–N and C–C peaks at 286.2 and 284.7 eV, respectively, corresponding to the methylammonium $CH_3NH_3^+$ cations (Fig. 4c). The non-shifting of Pb 4f, Br 3d, and C 1s peaks, with Cu-alloying, is consistent with the formation of $MAPbBr_3$ film as a major phase. In addition, Cu^{2+} cations embedded in the film are evident with the presence of Cu $2p_{3/2}$ at 932.9 eV[67] for 10% and 20% samples which are slightly shifted to lower binding energy at 932.7 eV for higher concentration Cu-alloyed perovskites (Fig. S9a, ESI†), revealing the difference in chemical structure nature of Cu^{2+} alloyed in perovskite which is consistent with XRD results. The formation of Cu-satellite structure at higher Cu-alloyed samples (Fig. 4d) indicates the presence of Cu^{2+} species, as expected.[68] Gradual increasing of Cu $2p_{3/2}$ peak area is a clear indication of increasing of copper concentration embedded in perovskite thin films upon alloying (Fig. S9b, ESI†). Notably, after incorporation of 50% Cu, the Br 3d, and C 1s peaks area is clearly changed which might be attributed to the Cu-rich secondary phase formation. Furthermore, new peaks at 141.4 eV and 136.6 eV are formed through the Pb 4f spectrum which might be assigned to the formation of Pb metal or the Pb occupation of the Cu-rich secondary phase interstitial positions.[69] The changes in peak area behavior for Pb and Br are depicted in Fig. S9c and d (ESI†).
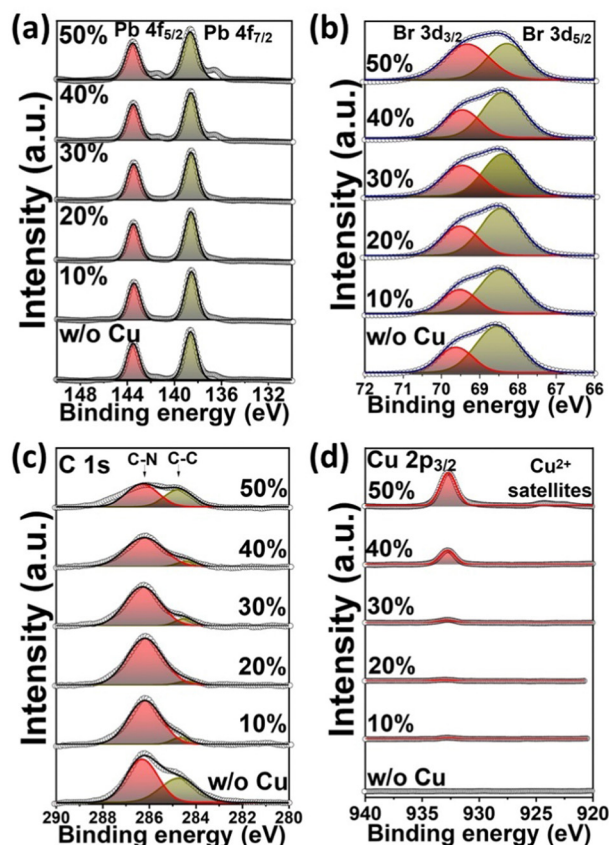
Fig. 4   XPS spectra of Pb4f (a), Br3d (b), C1s (c), and Cu2p (d), and Br3d (e) of Cu-alloyed MAPbBr$_3$ perovskite thin films.

The optical properties of the samples are evaluated by obtaining UV-Vis absorption spectra of the pristine and Cu-substituted MAPbBr$_3$ thin films (as illustrated in Fig. 5a). The absorption edges undergo a slight red-shifting with alloying of up to 40% Cu, and subsequently, a sudden and considerable red-shift (near-IR range) occurs for the 50% Cu-substituted sample. Tauc plots, Fig. 5b, and Fig. S10 (ESI†), show that the optical direct bandgaps of the perovskites are 2.32 eV for pristine MAPbBr$_3$, 2.31 eV for 10%, 2.31 eV for 20%, 2.29 eV for 30%, 2.28 eV for 40%, and 1.85 eV for 50% Cu-substituted MAPbBr$_3$ thin films. Tuning of the optical bandgap energies is consistent with the perovskite thin film color tuning (from yellowish orange to dark brown) with increasing Cu content. Moreover, the trend
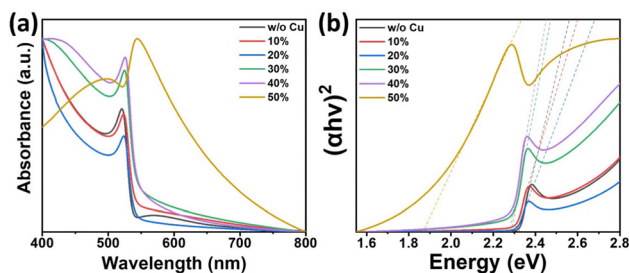

Fig. 5   (a and b) Absorption spectra, and direct bandgap estimation: Tauc plot, respectively, of Cu-alloyed MAPbBr$_3$ thin films.

observed for the absorption spectrum of the 50% Cu-substituted film is similar to that observed for Cu-based perovskite materials.[70] This may have resulted from the higher concentration of Cu-rich secondary phase in the 50% Cu-substituted film compared with the concentrations occurring in the other films. The inhomogeneous broadening of PL emission peaks with Cu-doping, as shown in Fig. S11a (ESI†), further confirms the heterogeneity of the doped films. The results revealed that 10% doping enhances room temperature PL emission of MAPbBr$_3$ (76% increase in PL peak area), as shown in Fig. S11b (ESI†). This may have resulted from the homogeneously distributed low-Cu-concentration doping effect of the 10% Cu perovskite thin film without secondary phase formation. However, further Cu-doping (of up to 50% doping) leads to quenching of the PL emission and 85% recovery of the pristine MAPbBr$_3$ PL emission (Fig. S11b, ESI†). Normalized PL spectra (Fig. S11c, ESI†) revealed that, with 50% Cu-doping, the PL shifts slightly (0.2 nm) to longer wavelength than those observed at other doping levels (Fig. S11d, ESI†).

Using the four-probe method, we measured the electrical conductivity of perovskite thin films as a function of Cu alloying, as shown in Fig. 6a. The conductivity increases significantly with alloying and the highest value is obtained for the 40% Cu-substituted thin film, owing possibly to the presence of homogeneously distributed secondary phases. Subsequently, the conductivity decreases slightly for the 50% Cu substituted material, consistent with the heterogeneously distributed Cu-rich new phase formed in this material (as depicted in Fig. 2f and Fig. S2, ESI†). The 40% Cu-substituted MAPbBr$_3$ thin film exhibits the highest dark electrical conductivity $(10.77 \times 10^{-4}\ \text{S cm}^{-1})$, which is nearly three orders of magnitude higher than that of the pristine MAPbBr$_3$ thin film $(4.10 \times 10^{-7}\ \text{S cm}^{-1})$. To evaluate the secondary phase stability, we measure the conductivity under the effect of temperature (temperature range: 300 K–110 K) for one cooling/heating (C/H) cycle. We first measure the conductivity upon cooling from room temperature (300 K) to 110 K, and then upon heating back from 110 K to 330 K. Fig. 6b shows the results of temperature-dependent conductivity measurements performed on pristine MAPbBr$_3$ where the conductivity decreases from $7.05 \times 10^{-8}\ \text{S cm}^{-1}$ at 300 K to $2.72 \times 10^{-8}\ \text{S cm}^{-1}$ at 110 K. The reverse behavior is observed upon heating, $i.e.$, increasing conductivity with slight hysteresis at temperatures ranging from 200 K to 220 K. This behavior may have resulted from a phase transition where the tetragonal structure at $T < 200$ K transforms into a cubic structure at $T > 220$ K.[71] Fig. 6c shows the results of the conductivity measurements performed on 40% Cu-MAPbBr$_3$. The conductivity decreases sharply from $1.16 \times 10^{-3}\ \text{S cm}^{-1}$ at 300 K to $2.06 \times 10^{-7}\ \text{S cm}^{-1}$ at 270 K and then decreases to $4.47 \times 10^{-8}\ \text{S cm}^{-1}$ at 110 K. Interestingly, upon heating, the 40% Cu sample behave like pristine MAPbBr$_3$ where the conductivity increases slightly to $2.66 \times 10^{-7}\ \text{S cm}^{-1}$ at 330 K. The cooling/heating cycle behavior of the 40% Cu samples can be attributed to a phase transition from the secondary hexagonal phase at room temperature (300 K) to the cubic phase at 270 K. The inset image shown in Fig. 6c reveals that, at
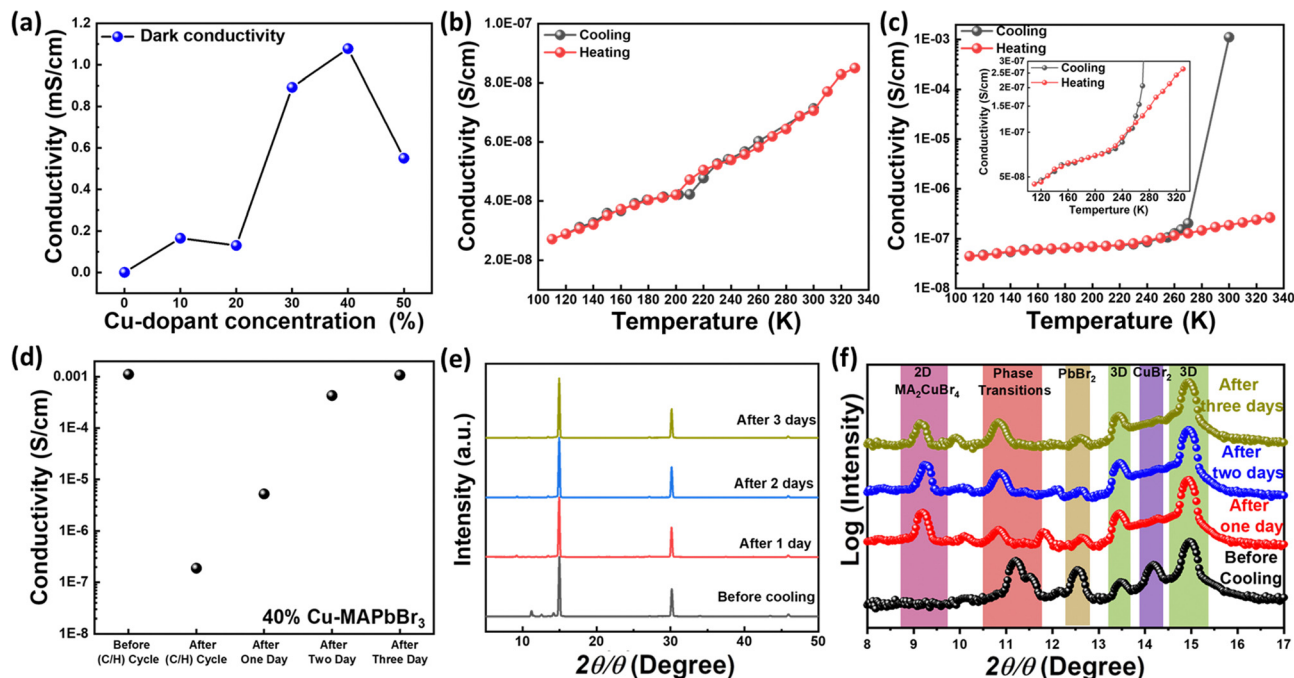
Fig. 6 (a) Conductivity of Cu-MAPbBr$_3$ perovskite thin films at room temperature. (b and c) Temperature-dependent conductivity of pristine MAPbBr$_3$ and 40% Cu-MAPbBr$_3$ perovskite thin films, respectively for one cooling/heating cycle. The inset in (c): zoom for low conductivity values. (d and e) Time-dependent conductivity and time-dependent XRD patterns, respectively, of 40% Cu-MAPbBr$_3$ perovskite thin film after cooling/heating cycle effect. (f) Plots on log scale for $2\theta = 8-17°$.

temperatures of 200–220 K, the same hysteresis occurs as the pristine perovskite (Fig. 6b), thereby confirming the occurrence of another phase transition to the tetragonal structure at $T < 200$ K. The Cu-alloyed perovskite thin film recovers its original conductivity value (1.08×10^{-3} S cm^{-1}) after three days (Fig. 6d). This indicates that, compared with the pristine material, the 40% Cu perovskite requires more time for re-formation of its more stable hexagonal secondary phase with its original higher conductivity value. The activation energy (E_a) can reflect the energy difference between the conduction band and the Fermi energy (or defect levels). E_a required for charge transport can be obtained from conductivity measurements based on the Arrhenius equation $S = S_0 \exp(-E_a/k_B T)$ where S, S_0, k_B, and T are the conductivity, a constant, the Boltzmann constant, and the absolute temperature, respectively. We obtained an E_a of 29 meV for pristine MAPbBr$_3$ and a considerably lower estimated value of 2 meV for the 40% Cu-substituted perovskite, as depicted in Fig. S12 (ESI†). The reduced E_a required for the alloyed perovskite may correspond to the change in Fermi energy or arising defect levels. This suggests that the carrier density increases with Cu-alloying where the presence of hexagonal secondary phases may play a crucial role in E_a reduction. For additional insight into the temperature-dependent conductivity behavior, the phase transitions in the 40% Cu-substituted perovskite are further tracked during three consecutive days of XRD measurements. The main cubic MAPbBr$_3$ cubic structure of the material is retained after one day of the (C/H) cycle (Fig. 6e). However, the XRD peak of the hexagonal secondary phase is shifted to lower 2θ than the initial values (Fig. 6f). This shifting is

accompanied by the appearance of a peak at $2\theta = 9.2°$, which corresponds to two-dimensional (2D) MA$_2$CuBr$_4$ perovskite.[64] Moreover, the XRD peak at $2\theta = 14.3°$, which is associated with the unreacted CuBr$_2$, disappears after the (C/H) cycle, thereby further confirming the formation of 2D Cu-based perovskite. This formation may have led to the aforementioned sudden decrease in the conductivity of the alloyed sample after the one-day (C/H) cycle. With the progression of the measurement, the XRD peak intensity of the MA$_2$CuBr$_4$ perovskite decreases, and the peak intensity of the hexagonal secondary phase increases. The direct dependence of the XRD peak intensity ratio (Iphase transitions/IMA$_2$CuBr$_4$) on time reveals that the hexagonal secondary phases are restored at the expense of 2D MA$_2$CuBr$_4$ perovskite (as depicted in Fig. S13, ESI†). Consequently, the original conductivity of the 40% Cu-substituted perovskite is restored after the three-day measurement period.

To determine the potential of pristine/alloyed perovskite thin films for optoelectronic devices, photocurrent measurements were performed as a function of the excitation wavelength (*i.e.*, the excitation photon energy). Two types of transitions are (in general) observed (Fig. 7a): type I is a band-to-band transition (*i.e.*, from valence band to conduction band), which requires higher excitation energy than the bandgap energy for photocarrier generation. Type II, which is a transition between a defect level and either the valence or conduction band, occurs with excitation energy either higher or lower than the bandgap energy for photocarrier generation.[72] Fig. 7b shows the normalized photocurrent spectra of both pristine and 40% Cu-substituted MAPbBr$_3$ thin films as a function of the excitation photon energy. When the
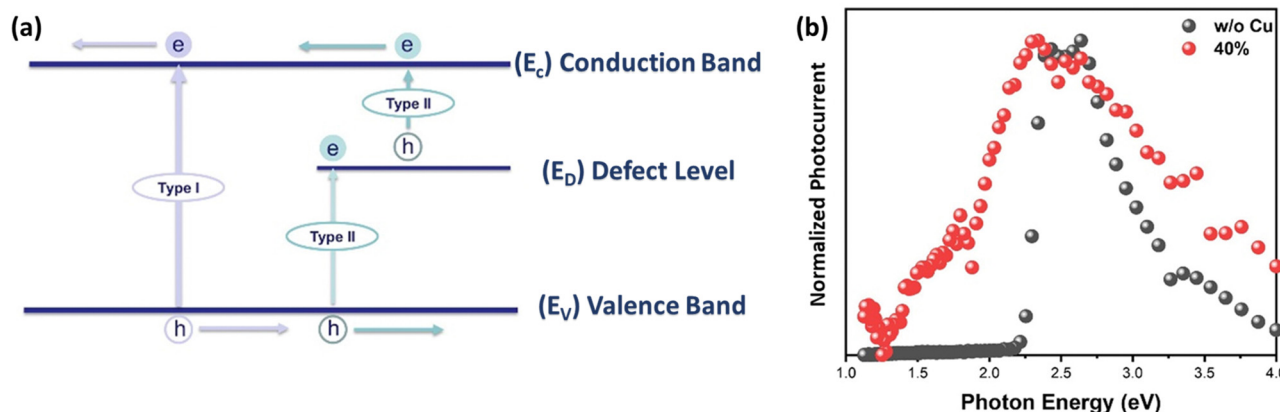
Fig. 7 (a) Graphical illustration of photo-excitation processes in Cu-alloyed MAPbBr$_3$ perovskite and (b) Photocurrent spectra of pristine MAPbBr$_3$ and 40% Cu-alloyed MAPbBr$_3$ thin films at room temperature.

energy of excitation with photons is higher than the bandgap, $E_{Ph} > E_g$, the photocurrent of each sample rises sharply (*i.e.*, intrinsic photocurrent generation occurs) despite the difference in alloying levels. Thereafter, the photocurrent decreases with increasing excitation photon energy. This may have resulted from the reduction in the penetration-depth (where carriers are generated at the perovskite surface), owing to rapid deterioration induced by the surface effect. It should be noted that, at higher energy, pristine perovskite reveals a higher surface recombination rate than that of 40% alloyed one, as shown in Fig. 7b, which might be due to the increasing of penetration depth upon Cu-alloying. No photocurrent generation occurs in pristine MAPbBr$_3$ subjected to excitation at the near-infrared region. However, band-carrier generation increases with increasing Cu-substituting level. This strongly suggests that sub-bandgap absorption levels (defect levels) are present in the Cu-alloyed samples. Furthermore, defect level-related photocurrent is generated (*i.e.* Type II transition) above the threshold energy (E_T), *i.e.*, 1.25 eV (a defect level is located at ∼1.25 eV below the conduction band (or above the valence band)). This defect level behavior has been observed previously.[72–75] The bandgaps of the perovskites are 2.24 eV for pristine MAPbBr$_3$, and 2.22 eV, 2.19 eV, 2.14 eV, 1.90 eV, and 1.78 eV for 10%, 20%, 30%, 40%, and 50% Cu-substituted MAPbBr$_3$ thin films, respectively (as depicted in Fig. S14, ESI†). These values correspond closely to the optical bandgaps obtained from the Tauc plots. Bandgap narrowing, with near IR carrier generation, makes Cu-alloyed MAPbBr$_3$ perovskite thin film a promising candidate for NIR Photodetectors[76] and other optoelectronic devices.[77] It should be hinted that the only MAPbBr$_3$ based photodetector, with narrow NIR-visible light dual-mode, was recently reported by Zhao *et al.*[76]

To gain further insight into Cu alloying of MAPbBr$_3$, first principles point defect simulations were performed (details about the formalism are presented in ESI†). Here, we designate cubic MAPbBr$_3$ as the parent phase and calculate the probability of Cu$_{Pb}$ extrinsic-defect formation. We employ a high Cu alloying concentration of 12.5% (5.59×10^{20} atoms per cm^3) in the model. The findings reported in the literature regarding the oxidation state of Cu substituted into halide perovskites are inconsistent[72,78–81] (both +1 and +2 charge states have been reported). In our calculation, we consider both +1 (Cu$_{Pb}^{-1}$) and +2 (Cu$_{Pb}^{0}$) oxidation states of Cu, for modeling the Pb-replacing perovskite octahedra. The simulation results (Fig. 8a and b) revealed that, in the highly p-alloyed system (when the Fermi level is close to VBM), the neutral state is more stable than the other states. However, in the n-alloyed samples, Cu behaves as an acceptor type defect. Moreover, Cu substitution creates a charge imbalance in the system and can therefore trigger the formation of intrinsic secondary donor defects that compensate for this imbalance. The results reported in the literature indicate that, in the case of MAPbBr$_3$, the most probable intrinsic donors are a Br vacancy (v_{Br}) and an MA interstitial (MA$_i$).[82] Consequently, in this study, we consider Cu$_{Pb}$, v_{Br}, and MA$_i$ individual point defects as well as Cu$_{Pb}$ + v_{Br} and Cu$_{Pb}$ + MA$_i$ defect complexes with different charge states. With Cu alloying, the octahedral geometry changes substantially (mainly due to size mismatch between Cu and Pb), and as such we consider Br vacancies at two different (namely axial and equatorial) sites of the octahedron. We incorporate the effect of chemical growth environment by considering the chemical potentials of the constituent elements.

To elaborate, we draw a compositional phase diagram of MAPbBr$_3$ (Fig. 8c and d) considering all the secondary phases from OQMD. We choose two corner points (chemical potential values to be used in defect formation energy calculation) of the diagram, which represent Pb rich/Br poor and Pb poor/Br rich conditions. The chemical potential of Cu is kept as rich as possible (for consistency with our experimental conditions) by considering elemental Cu and CuBr$_2$ phases (experimental precursor) (additional details on the chosen chemical potential values are presented in the experimental section). To validate our methodology, we compare our calculated formation energies and charge transition levels of two intrinsic defects (namely v_{Br} and MA$_i$) with values reported in the literature, and a reasonable agreement is realized.[83] The point defect diagrams (Fig. 8a and b) indicate that Cu alloying will be more likely under Pb poor/Br rich (p-type) growth conditions than under Pb rich/Br poor growth conditions. It is likely that the
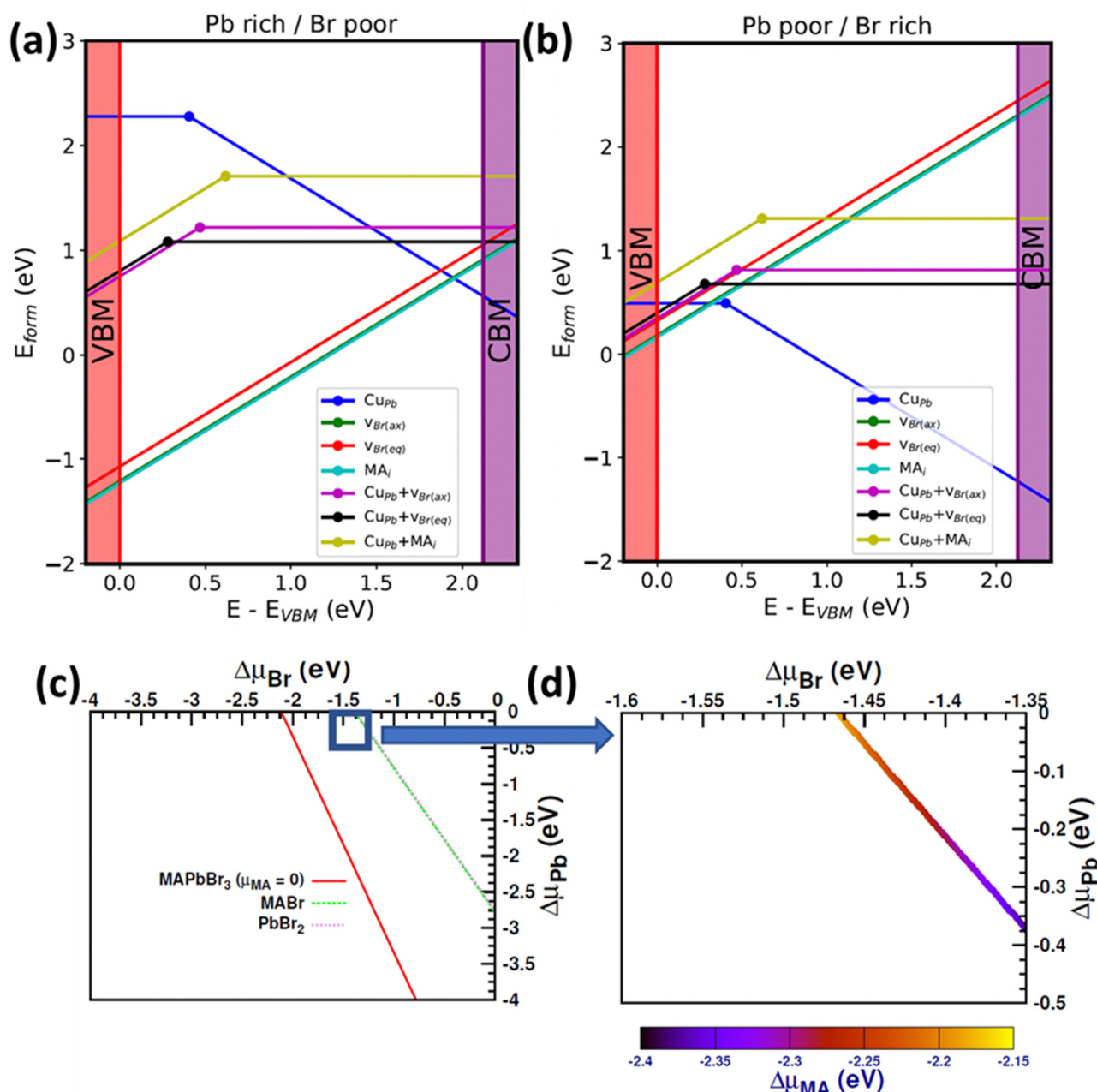
Fig. 8 Formation energies of simulated point defects with respect to Fermi level associated with two different growth environments (Pb rich/Br poor (a) and Pb poor/Br rich (b)). Defect charge states (q) are the slope of the curves (we performed simulations for $q = -1$, 0, and +1) and charge transition points are denoted by circles. Red- and purple-shaded regions represent the valence band (and below) and conduction band (and above), respectively. (c) Compositional phase diagram showing competing secondary phases of MAPbBr$_3$. (d) Zoomed view of the region enclosed in the box in (c).

Fermi level pinning will be near CBM (VBM) under Pb rich/Br poor (Pb poor/Br rich) conditions. In this case, the formation energy of compensating intrinsic defects and defect complexes remains close to that of Cu$_{Pb}$ in both chemical environments. This means that defect compensation is likely for Cu alloying under these conditions. From our analysis, v_{Br} turns out to be the most probable compensating defect. We also calculate the defect complex binding energy ($E_b = E_{form}(Cu_{Pb} + v_{Br}) - E_{form}(Cu_{Pb}) - E_{form}(v_{Br})$) at different Fermi levels. Our calculated value lies between -0.41 eV (E_F at VBM) and -0.53 eV (E_F at CBM),

indicating that formation of the Cu$_{Pb}$ + v_{Br} defect complex is quite likely. However, for Cu$_{Pb}$ + MA$_i$, E_b lies between 0.04 eV (E_F at VBM) and 0.26 eV (E_F at CBM), suggesting a moderate to low formation tendency of this complex. Moderate to deep-level (0.2–0.5 eV above VBM) charge transitions are observed for Cu$_{Pb}$ and the associated defect complexes.

We evaluate the effect of Cu alloying (and possible defect complexes) on the electronic properties of MAPbBr$_3$ by plotting the orbital projected density of states for 50% Cu substituted MAPbBr3 with (and without) a Br vacancy, as shown in Fig. 9.
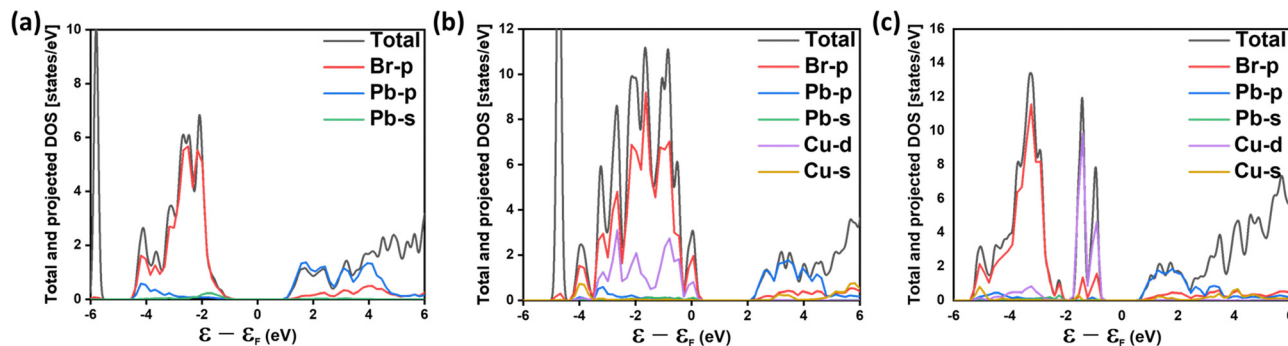
Fig. 9 Atomic orbital projected density of states for (a) pure MAPbBr$_3$, (b) 50% Cu alloyed MAPbBr$_3$, and (c) 50% Cu alloyed MAPbBr$_3$ with a Br vacancy.

With only Cu alloying at Pb sites, Fig. 9b, we observe that the effective gap decreases slightly (from 2.12 eV to 1.90 eV) compared with that of the pristine material, as depicted in Fig. 9a. In Fig. 9c, with the formation of Br vacancy ($Cu_{Pb} + v_{Br}$, defect complex), the presence of localized defect states can be observed within the pristine bandgap, formed by Cu-d and Br-p orbitals. This may explain the experimentally observed sub-bandgap absorption with 40% Cu alloying (Fig. 7b).

Experimental

Characterization

Scanning electron microscopy (SEM) with energy dispersive spectroscopy (EDS; JEOL, JEM-2100F) was used to determine the Pb/Cu atomic weight percentages and to obtain the elemental mapping of the perovskite samples. The results confirmed that the number of grain boundaries increased, and a Cu-rich secondary phase formed during Cu doping. The photoluminescence of the perovskite was characterized *via* Raman spectroscopy (JASCO, NRS4500 NMDS) performed with 532-nm excitation (green) lasers. Absorption measurements performed *via* ultraviolet-visible near-infrared (UV-Vis-NIR) spectroscopy (JASCO, V-670) were used to estimate the bandgap from a Tauc plot. X-ray (Rigaku XRD) reflection data was measured at a wavelength of 1.5406 Å. X-ray photoelectron spectroscopy (XPS) was characterized on JEOL JPS-9030 with X-ray source of Mg K Alfa (Monochromatic) with 25 mA beam current and 12 kV. In addition, electrical measurements were conducted using a source meter (ADCMT, 6245) with a temperature controller installed in a four-probe station (Riko International Ltd.). The sample temperature was controlled by cooling the sample stage of the four-probe station using liquid nitrogen with a temperature controller under vacuum condition ($\sim 5.0 \times 10^{-2}$ Pa). Photocurrent measurements at room temperature were performed in the station using a source meter (KEITHLEY, 2611A) with monochromatic light illumination. The wavelength of this illumination was controlled by a monochromator (BUNKOKEIKI, SM2-25).

Computational details

First-principles calculations were performed using Density Functional Theory (DFT)[84] within the Projector-Augmented Wave (PAW)[85] formalism as implemented in a GPAW[86] code combined with an Atomic Simulation Environment (ASE).[87] A plane wave cutoff energy of 800 eV and *k*-point density of 6 Å^{-1} (12 Å^{-1}) were employed for geometry optimization (ground state calculations). Electronic structure calculations were performed using a Perdew–Burke–Ernzerhof (PBE)[88] exchange–correlation functional. In addition, a $2 \times 2 \times 2$ (96 atoms) supercell of the MAPbBr$_3$ cubic unit cell was used for point defect calculations. A *k*-point density of 3.5 Å^{-1} (7 Å^{-1}) was used for sampling the Brillouin zone for the supercells. Forces were converged up to 0.02 eV Å^{-1} for the defect calculations, where the supercell size was kept fixed. Compositional phase diagrams were obtained using a CPLAP code.[89] The computational workflow was constructed using the Atomic Simulation Recipes (ASR)[90] and executed using the My Queue[91] task scheduler frontend.

Conclusions

We have demonstrated that Cu alloying of MAPbBr$_3$ thin films leads to an increase in the grain boundary area with the formation of Cu-rich secondary phases. The formation of hexagonal perovskite secondary phases is proposed to be more likely in the Cu-alloyed materials than in the non-alloyed materials as supported by calculated convex hull energies. Bandgap decreases slightly with Cu alloying until 40% concentration. A substantially reduced bandgap is observed in 50% Cu-substituted thin film which can be attributed to the presence of Cu-rich secondary phase. Intriguingly, the activation energy of the 40%Cu-substituted perovskite is considerably lower than that of the pristine material, and the conductivity is significantly higher ($10^3 \times$). In addition, photocurrent carriers are generated in the NIR region of the alloyed material. Based on point defect simulation results, we propose that a compensating Br vacancy will form with alloying and the associated defect complex may induce defect states inside the pristine bandgap, which may explain the experimentally observed optical signature.

Author contributions

Amr Elattar conceived the manuscript's concept and designed the experiments. Amr Elattar, Kodai Nakao, and Kosei Tsutsumi

synthesized the materials and conducted structural, electrical, and optical characterizations. Theoretical part was performed and wrote by Jiban Kangsabanik. The first manuscript was written by Amr Elattar and. At various phases, the writers discussed the findings and provided feedback on the manuscript. Kristian S. Thygesen led the assessment of theoretical part. Yasuhiko Hayashi coordinated the entire project.

Conflicts of interest

There are no conflicts to declare.

Acknowledgements

References

1 S. D. Stranks, G. E. Eperon, G. Grancini, C. Menelaou, M. J. P. Alcocer, T. Leijtens, L. M. Herz, A. Petrozza and H. J. Snaith, Electron-Hole Diffusion Lengths Exceeding 1 Micrometer in an Organometal Trihalide Perovskite Absorber, *Science*, 2013, **342**, 341 LP–344 LP.

2 N. J. Jeon, J. H. Noh, Y. C. Kim, W. S. Yang, S. Ryu and S. Il, Seok, Solvent engineering for high-performance inorganic–organic hybrid perovskite solar cells, *Nat. Mater.*, 2014, **13**, 897–903.

3 N. J. Jeon, J. H. Noh, W. S. Yang, Y. C. Kim, S. Ryu, J. Seo and S. Il, Seok, Compositional engineering of perovskite materials for high-performance solar cells, *Nature*, 2015, **517**, 476–480.

4 T. Chen, W.-L. Chen, B. J. Foley, J. Lee, J. P. C. Ruff, J. Y. P. Ko, C. M. Brown, L. W. Harriger, D. Zhang, C. Park, M. Yoon, Y.-M. Chang, J. J. Choi and S.-H. Lee, Origin of long lifetime of band-edge charge carriers in organic–inorganic lead iodide perovskites, *Proc. Natl. Acad. Sci. U. S. A.*, 2017, **114**, 7519 LP–7524 LP.

5 X. Yang, Y. Fu, R. Su, Y. Zheng, Y. Zhang, W. Yang, M. Yu, P. Chen, Y. Wang, J. Wu, D. Luo, Y. Tu, L. Zhao, Q. Gong and R. Zhu, Superior Carrier Lifetimes Exceeding 6 μs in Polycrystalline Halide Perovskites, *Adv. Mater.*, 2020, **32**, 2002585.

6 L. Qiao, W.-H. Fang, R. Long and O. V. Prezhdo, Photoinduced Dynamics of Charge Carriers in Metal Halide Perovskites from an Atomistic Perspective, *J. Phys. Chem. Lett.*, 2020, **11**, 7066–7082.

7 W. Li, A. S. Vasenko, J. Tang and O. V. Prezhdo, Anharmonicity Extends Carrier Lifetimes in Lead Halide Perovskites at Elevated Temperatures, *J. Phys. Chem. Lett.*, 2019, **10**, 6219–6226.

8 J. Jiang, X. Sun, X. Chen, B. Wang, Z. Chen, Y. Hu, Y. Guo, L. Zhang, Y. Ma, L. Gao, F. Zheng, L. Jin, M. Chen, Z. Ma, Y. Zhou, N. P. Padture, K. Beach, H. Terrones, Y. Shi, D. Gall, T.-M. Lu, E. Wertz, J. Feng and J. Shi, Carrier lifetime enhancement in halide perovskite via remote epitaxy, *Nat. Commun.*, 2019, **10**, 4145.

9 E. L. Unger, L. Kegelmann, K. Suchan, D. Sörell, L. Korte and S. Albrecht, Roadmap and roadblocks for the band gap tunability of metal halide perovskites, *J. Mater. Chem. A*, 2017, **5**, 11401–11409.

10 Y. El Ajjouri, A. M. Igual-Muñoz, M. Sessolo, F. Palazon and H. J. Bolink, Tunable Wide-Bandgap Monohalide Perovskites, *Adv. Opt. Mater.*, 2020, **8**, 2000423.

11 R. J. Sutton, G. E. Eperon, L. Miranda, E. S. Parrott, B. A. Kamino, J. B. Patel, M. T. Hörantner, M. B. Johnston, A. A. Haghighirad, D. T. Moore and H. J. Snaith, Bandgap-Tunable Cesium Lead Halide Perovskites with High Thermal Stability for Efficient Solar Cells, *Adv. Energy Mater.*, 2016, **6**, 1502458.

12 L. Wang, G. D. Yuan, R. F. Duan, F. Huang, T. B. Wei, Z. Q. Liu, J. X. Wang and J. M. Li, Tunable bandgap in hybrid perovskite $CH_3NH_3Pb(Br_{3−y}X_y)$ single crystals and photodetector applications, *AIP Adv.*, 2016, **6**, 45115.

13 Z. Yang, Z. Yu, H. Wei, X. Xiao, Z. Ni, B. Chen, Y. Deng, S. N. Habisreutinger, X. Chen, K. Wang, J. Zhao, P. N. Rudd, J. J. Berry, M. C. Beard and J. Huang, Enhancing electron diffusion length in narrow-bandgap perovskites for efficient monolithic perovskite tandem solar cells, *Nat. Commun.*, 2019, **10**, 4498.

14 G. D. Tainter, M. T. Hörantner, L. M. Pazos-Outón, R. D. Lamboll, H. Āboliņš, T. Leijtens, S. Mahesh, R. H. Friend, H. J. Snaith, H. J. Joyce and F. Deschler, Long-Range Charge Extraction in Back-Contact Perovskite Architectures via Suppressed Recombination, *Joule*, 2019, **3**, 1301–1313.

15 K. K. Chauhan, S. Prodhan, D. Ghosh, P. Waghale, S. Bhattacharyya, P. K. Dutta and P. K. Datta, Long Carrier Diffusion Length and Slow Hot Carrier Cooling in Thin Film Mixed Halide Perovskite, *IEEE J. Photovolt.*, 2020, **10**, 803–810.

16 M. C. Gélvez-Rueda, M. B. Fridriksson, R. K. Dubey, W. F. Jager, W. van der Stam and F. C. Grozema, Overcoming the exciton binding energy in two-dimensional perovskite nanoplatelets by attachment of conjugated organic chromophores, *Nat. Commun.*, 2020, **11**, 1901.

17 K. Galkowski, A. Mitioglu, A. Miyata, P. Plochocka, O. Portugall, G. E. Eperon, J. T.-W. Wang, T. Stergiopoulos, S. D. Stranks, H. J. Snaith and R. J. Nicholas, Determination of the exciton binding energy and effective masses for methylammonium and formamidinium lead tri-halide perovskite semiconductors, *Energy Environ. Sci.*, 2016, **9**, 962–970.

18 M. Baranowski and P. Plochocka, Excitons in Metal-Halide Perovskites, *Adv. Energy Mater.*, 2020, **10**, 1903659.

19 X. Chen, H. Lu, Y. Yang and M. C. Beard, Excitonic Effects in Methylammonium Lead Halide Perovskites, *J. Phys. Chem. Lett.*, 2018, **9**, 2595–2603.

20 C. Zhang, Y. Wang, X. Lin, T. Wu, Q. Han, Y. Zhang and L. Han, Effects of A site doping on the crystallization of perovskite films, *J. Mater. Chem. A*, 2021, **9**, 1372–1394.

21 M. Qin, H. Xue, H. Zhang, H. Hu, K. Liu, Y. Li, Z. Qin, J. Ma, H. Zhu, K. Yan, G. Fang, G. Li, U.-S. Jeng, G. Brocks, S. Tao and X. Lu, Precise Control of Perovskite Crystallization Kinetics via Sequential A-Site Doping, *Adv. Mater.*, 2020, **32**, 2004630.

22 S. Xu, X. Ding, H. Shi, X. Zhang, X. Sun, N. Ji, X. Zhang and Z. Zhang, EA-Directing Formamidinium-Based Perovskite Microwires with A-Site Doping, *ACS Omega*, 2021, **6**, 7157–7164.

23 S. Wang, H. Liu, H. Bala, B. Zong, L. Huang, Z. Guo, W. Fu, B. Zhang, G. Sun, J. Cao and Z. Zhang, A highly stable hole-conductor-free $Cs_xMA_{1-x}PbI_3$ perovskite solar cell based on carbon counter electrode, *Electrochim. Acta*, 2020, **335**, 135686.

24 T. Binyamin, L. Pedesseau, S. Remennik, A. Sawahreh, J. Even and L. Etgar, Fully Inorganic Mixed Cation Lead Halide Perovskite Nanoparticles: A Study at the Atomic Level, *Chem. Mater.*, 2020, **32**, 1467–1474.

25 D. P. McMeekin, G. Sadoughi, W. Rehman, G. E. Eperon, M. Saliba, M. T. Hörantner, A. Haghighirad, N. Sakai, L. Korte, B. Rech, M. B. Johnston, L. M. Herz and H. J. Snaith, A mixed-cation lead mixed-halide perovskite absorber for tandem solar cells, *Science*, 2016, **351**, 151 LP–155 LP.

26 W. Rehman, D. P. McMeekin, J. B. Patel, R. L. Milot, M. B. Johnston, H. J. Snaith and L. M. Herz, Photovoltaic mixed-cation lead mixed-halide perovskites: links between crystallinity, photo-stability and electronic properties, *Energy Environ. Sci.*, 2017, **10**, 361–369.

27 D. J. Kubicki, D. Prochowicz, A. Hofstetter, S. M. Zakeeruddin, M. Grätzel and L. Emsley, Phase Segregation in Potassium-Doped Lead Halide Perovskites from ^{39}K Solid-State NMR at 21.1 T, *J. Am. Chem. Soc.*, 2018, **140**, 7232–7238.

28 Y. Zhou, J. Chen, O. M. Bakr and H.-T. Sun, Metal-Doped Lead Halide Perovskites: Synthesis, Properties, and Optoelectronic Applications, *Chem. Mater.*, 2018, **30**, 6589–6613.

29 Z. Tang, T. Bessho, F. Awai, T. Kinoshita, M. M. Maitani, R. Jono, T. N. Murakami, H. Wang, T. Kubo, S. Uchida and H. Segawa, Hysteresis-free perovskite solar cells made of potassium-doped organometal halide perovskite, *Sci. Rep.*, 2017, **7**, 12183.

30 Q. Liu, M.-G. Ju and W. Liang, Potassium doping-induced variations in the structures and photoelectric properties of a $MAPbI_3$ perovskite and a $MAPbI_3/TiO_2$ junction, *Phys. Chem. Chem. Phys.*, 2020, **22**, 20553–20561.

31 B. Luo, F. Li, K. Xu, Y. Guo, Y. Liu, Z. Xia and J. Z. Zhang, B-Site doped lead halide perovskites: synthesis, band engineering, photophysics, and light emission applications, *J. Mater. Chem. C*, 2019, **7**, 2781–2808.

32 X. Ge, X. Qu, L. He, Y. Sun, X. Guan, Z. Pang, C. Wang, L. Yang, F. Wang and F. Rosei, 3D low toxicity Cu–Pb binary perovskite films and their photoluminescent/photovoltaic performance, *J. Mater. Chem. A*, 2019, **7**, 27225–27235.

33 J. Zhang, X. Gan, H. Sun, H. Yuan, X. Lu, Z. Hu and Y. Zhu, Pb-Site Doping of Lead Halide Perovskites for Efficient Solar Cells, *Sol. RRL*, 2020, **4**, 1900227.

34 W. Liu, L. Chu, N. Liu, Y. Ma, R. Hu, Y. Weng, H. Li, J. Zhang, X. Li and W. Huang, Efficient perovskite solar cells fabricated by manganese cations incorporated in hybrid perovskites, *J. Mater. Chem. C*, 2019, **7**, 11943–11952.

35 M. N. Islam, M. A. Hadi and J. Podder, Influence of Ni doping in a lead-halide and a lead-free halide perovskites for optoelectronic applications, *AIP Adv.*, 2019, **9**, 125321.

36 S. Thawarkar, P. J. S. Rana, R. Narayan and S. P. Singh, Ni-Doped $CsPbBr_3$ Perovskite: Synthesis of Highly Stable Nanocubes, *Langmuir*, 2019, **35**, 17150–17155.

37 S.-H. Chan, M.-C. Wu, K.-M. Lee, W.-C. Chen, T.-H. Lin and W.-F. Su, Enhancing perovskite solar cell performance and stability by doping barium in methylammonium lead halide, *J. Mater. Chem. A*, 2017, **5**, 18044–18052.

38 A. M. Ulatowski, A. D. Wright, B. Wenger, L. R. V. Buizza, S. G. Motti, H. J. Eggimann, K. J. Savill, J. Borchert, H. J. Snaith, M. B. Johnston and L. M. Herz, Charge-Carrier Trapping Dynamics in Bismuth-Doped Thin Films of $MAPbBr_3$ Perovskite, *J. Phys. Chem. Lett.*, 2020, **11**, 3681–3688.

39 A. L. Abdelhady, M. I. Saidaminov, B. Murali, V. Adinolfi, O. Voznyy, K. Katsiev, E. Alarousu, R. Comin, I. Dursun, L. Sinatra, E. H. Sargent, O. F. Mohammed and O. M. Bakr, Heterovalent Dopant Incorporation for Bandgap and Type Engineering of Perovskite Crystals, *J. Phys. Chem. Lett.*, 2016, **7**, 295–301.

40 R. Meng, G. Wu, J. Zhou, H. Zhou, H. Fang, M. A. Loi and Y. Zhang, Understanding the Impact of Bismuth Heterovalent Doping on the Structural and Photophysical Properties of $CH_3NH_3PbBr_3$ Halide Perovskite Crystals with Near-IR Photoluminescence, *Chem. – Eur. J.*, 2019, **25**, 5480–5488.

41 K. Yamada, H. Sera, S. Sawada, H. Tada, T. Okuda and H. Tanaka, Reconstructive Phase Transformation and Kinetics of $Cs_3Sb_2I_9$ by Means of Rietveld Analysis of X-Ray Diffraction and ^{127}I NQR, *J. Solid State Chem.*, 1997, **134**, 319–325.

42 M. Yavari, F. Ebadi, S. Meloni, Z. S. Wang, T. C.-J. Yang, S. Sun, H. Schwartz, Z. Wang, B. Niesen, J. Durantini, P. Rieder, K. Tvingstedt, T. Buonassisi, W. C. H. Choy, A. Filippetti, T. Dittrich, S. Olthof, J.-P. Correa-Baena and W. Tress, How far does the defect tolerance of lead-halide perovskites range? The example of Bi impurities introducing efficient recombination centers, *J. Mater. Chem. A*, 2019, **7**, 23838–23853.

43 Y. Yamada, M. Hoyano, R. Akashi, K. Oto and Y. Kanemitsu, Impact of Chemical Doping on Optical Responses in Bismuth-Doped $CH_3NH_3PbBr_3$ Single Crystals: Carrier Lifetime and Photon Recycling, *J. Phys. Chem. Lett.*, 2017, **8**, 5798–5803.

44 S. Rong, Y. Xiao, J. Jiang, Q. Zeng and Y. Li, Strongly Enhanced Photoluminescence and Photoconductivity in Erbium-Doped $MAPbBr_3$ Single Crystals, *J. Phys. Chem. C*, 2020, **124**, 8992–8998.

45 J. Gong, M. Yang, D. Rebollar, J. Rucinski, Z. Liveris, K. Zhu and T. Xu, Divalent Anionic Doping in Perovskite Solar Cells for Enhanced Chemical Stability, *Adv. Mater.*, 2018, **30**, 1800973.

46 M. Karlsson, Z. Yi, S. Reichert, X. Luo, W. Lin, Z. Zhang, C. Bao, R. Zhang, S. Bai, G. Zheng, P. Teng, L. Duan, Y. Lu, K. Zheng, T. Pullerits, C. Deibel, W. Xu, R. Friend and F. Gao, Mixed halide perovskites for spectrally stable and high-efficiency blue light-emitting diodes, *Nat. Commun.*, 2021, **12**, 361.

47 H. F. Zarick, N. Soetan, W. R. Erwin and R. Bardhan, Mixed halide hybrid perovskites: a paradigm shift in photovoltaics, *J. Mater. Chem. A*, 2018, **6**, 5507–5537.

48 P. Nandi, Z. Li, Y. Kim, T. K. Ahn, N.-G. Park and H. Shin, Stabilizing Mixed Halide Lead Perovskites against Photo-induced Phase Segregation by A-Site Cation Alloying, *ACS Energy Lett.*, 2021, **6**, 837–847.

49 Z. Chen, G. Brocks, S. Tao and P. A. Bobbert, Unified theory for light-induced halide segregation in mixed halide perovskites, *Nat. Commun.*, 2021, **12**, 2687.

50 L. Lei, Q. Dong, K. Gundogdu and F. So, Metal Halide Perovskites for Laser Applications, *Adv. Funct. Mater.*, 2021, **31**, 2010144.

51 S. Das, S. Gholipour and M. Saliba, Perovskites for Laser and Detector Applications, *Energy Environ. Mater.*, 2019, **2**, 146–153.

52 T. S. Kao, Y.-H. Hong, K.-B. Hong and T.-C. Lu, Perovskite random lasers: a tunable coherent light source for emerging applications, *Nanotechnology*, 2021, **32**, 282001.

53 W. Sun, Y. Liu, G. Qu, Y. Fan, W. Dai, Y. Wang, Q. Song, J. Han and S. Xiao, Lead halide perovskite vortex micro-lasers, *Nat. Commun.*, 2020, **11**, 4862.

54 H. Jing, R. Peng, R.-M. Ma, J. He, Y. Zhou, Z. Yang, C.-Y. Li, Y. Liu, X. Guo, Y. Zhu, D. Wang, J. Su, C. Sun, W. Bao and M. Wang, Flexible Ultrathin Single-Crystalline Perovskite Photodetector, *Nano Lett.*, 2020, **20**, 7144–7151.

55 C. Li, H. Wang, F. Wang, T. Li, M. Xu, H. Wang, Z. Wang, X. Zhan, W. Hu and L. Shen, Ultrafast and broadband photodetectors based on a perovskite/organic bulk hetero-junction for large-dynamic-range imaging, *Light: Sci. Appl.*, 2020, **9**, 31.

56 J. Deng, J. Xun, Y. Qin, M. Li and R. He, Blue-emitting NH_4^+-doped $MAPbBr_3$ perovskite quantum dots with near unity quantum yield and super stability, *Chem. Commun.*, 2020, **56**, 11863–11866.

57 R. Li, S. Chen, X. Li, G. Yin, Y. Gong, J. Yu, G. Pang, J. Liu, Y. Liu, Z. Ni, L. Zhang, R. Chen and H.-L. Wang, Zn doped MAPbBr3 single crystal with advanced structural and optical stability achieved by strain compensation, *Nanoscale*, 2020, **12**, 3692–3700.

58 Y. Yamada, M. Hoyano, K. Oto and Y. Kanemitsu, Effects of Impurity Doping on Photoluminescence Properties of $APbX_3$ Lead Halide Perovskites, *Phys. Status Solidi B*, 2019, **256**, 1800545.

59 C. C. Stoumpos, C. D. Malliakas and M. G. Kanatzidis, Semiconducting Tin and Lead Iodide Perovskites with Organic Cations: Phase Transitions, High Mobilities, and Near-Infrared Photoluminescent Properties, *Inorg. Chem.*, 2013, **52**, 9019–9038.

60 P. Gratia, I. Zimmermann, P. Schouwink, J.-H. Yum, J.-N. Audinot, K. Sivula, T. Wirtz and M. K. Nazeeruddin, The Many Faces of Mixed Ion Perovskites: Unraveling and Understanding the Crystallization Process, *ACS Energy Lett.*, 2017, **2**, 2686–2693.

61 J. Tian, D. B. Cordes, A. M. Z. Slawin, E. Zysman-Colman and F. D. Morrison, Progressive Polytypism and Bandgap Tuning in Azetidinium Lead Halide Perovskites, *Inorg. Chem.*, 2021, **60**, 12247–12254.

62 L. S. Ramsdell, Studies on silicon carbide, *Am. Mineral.*, 1947, **32**, 64–82.

63 K.-H. Wang, L.-C. Li, M. Shellaiah and K. Wen, Sun, Structural and Photophysical Properties of Methylammonium Lead Tri-bromide ($MAPbBr_3$) Single Crystals, *Sci. Rep.*, 2017, 7, 13643.

64 A. Elattar, H. Suzuki, R. Mishima, K. Nakao, H. Ota, T. Nishikawa, H. Inoue, A. K. K. Kyaw and Y. Hayashi, Single crystal of two-dimensional mixed-halide copper-based per-ovskites with reversible thermochromism, *J. Mater. Chem. C*, 2021, **9**, 3264–3270.

65 J. E. Saal, S. Kirklin, M. Aykol, B. Meredig and C. Wolverton, Materials Design and Discovery with High-Throughput Density Functional Theory: The Open Quantum Materials Database (OQMD), *JOM*, 2013, **65**, 1501–1509.

66 K. Lin, J. Xing, L. N. Quan, F. P. G. de Arquer, X. Gong, J. Lu, L. Xie, W. Zhao, D. Zhang, C. Yan, W. Li, X. Liu, Y. Lu, J. Kirman, E. H. Sargent, Q. Xiong and Z. Wei, Perovskite light-emitting diodes with external quantum efficiency exceeding 20 per cent, *Nature*, 2018, **562**, 245–248.

67 P. Pandey, N. Sharma, R. A. Panchal, S. W. Gosavi and S. Ogale, Realization of High Capacity and Cycling Stability in Pb-Free A_2CuBr_4 (A = CH_3NH_3/Cs, 2 D/3 D) Perovskite-Based Li-Ion Battery Anodes, *ChemSusChem*, 2019, **12**, 3742–3746.

68 P. Yang, G. Liu, B. Liu, X. Liu, Y. Lou, J. Chen and Y. Zhao, All-inorganic Cs_2CuX_4 (X = Cl, Br, and Br/I) perovskite quantum dots with blue-green luminescence, *Chem. Commun.*, 2018, **54**, 11638–11641.

69 N. Li, C. Cheng, H. Wei, H. Liu, X. Li, W. Li and L. Wang, Enhanced efficiency and stability of inverted perovskite solar cells by interfacial engineering with alkyl bisphospho-nic molecules, *RSC Adv.*, 2017, **7**, 42105–42112.

70 D. Cortecchia, H. A. Dewi, J. Yin, A. Bruno, S. Chen, T. Baikie, P. P. Boix, M. Grätzel, S. Mhaisalkar, C. Soci and N. Mathews, Lead-Free $MA_2CuCl_xBr_{4-x}$ Hybrid Perovskites, *Inorg. Chem.*, 2016, **55**, 1044–1052.

71 Y. Liu, H. Lu, J. Niu, H. Zhang, S. Lou, C. Gao, Y. Zhan, X. Zhang, Q. Jin and L. Zheng, Temperature-dependent photoluminescence spectra and decay dynamics of $MAPbBr_3$ and $MAPbI_3$ thin films, *AIP Adv.*, 2018, **8**, 95108.

72 F. Ji, Y. Huang, F. Wang, L. Kobera, F. Xie, J. Klarbring, S. Abbrent, J. Brus, C. Yin, S. I. Simak, I. A. Abrikosov, I. A. Buyanova, W. M. Chen and F. Gao, Near-Infrared Light-Responsive Cu-Doped $Cs_2AgBiBr_6$, *Adv. Funct. Mater.*, 2020, **30**, 2005521.

73 C. B. Simmons, A. J. Akey, J. P. Mailoa, D. Recht, M. J. Aziz and T. Buonassisi, Enhancing the Infrared Photoresponse of Silicon by Controlling the Fermi Level Location within an Impurity Band, *Adv. Funct. Mater.*, 2014, **24**, 2852–2858.

74 J. P. Mailoa, A. J. Akey, C. B. Simmons, D. Hutchinson, J. Mathews, J. T. Sullivan, D. Recht, M. T. Winkler, J. S. Williams, J. M. Warrender, P. D. Persans, M. J. Aziz and T. Buonassisi, Room-temperature sub-band gap optoelectronic response of hyperdoped silicon, *Nat. Commun.*, 2014, **5**, 3011.

75 M. K. Kavitha, K. B. Jinesh, R. Philip, P. Gopinath and H. John, Defect engineering in ZnO nanocones for visible photoconductivity and nonlinear absorption, *Phys. Chem. Chem. Phys.*, 2014, **16**, 25093–25100.

76 J. Zhao, X. Wang, Y. Xu, Y. Pan, Y. Li, J. Chen, Q. Li, X. Zhang, Z. Zhu, Z. Zhao, E. E. Elemike, D. C. Onwudiwe, B. S. Bae, S. bin Shafie and W. Lei, Electrically Modulated Near-Infrared/Visible Light Dual-Mode Perovskite Photodetectors, *ACS Appl. Mater. Interfaces*, 2022, **14**, 25824–25833.

77 N. J. Jeon, J. H. Noh, W. S. Yang, Y. C. Kim, S. Ryu, J. Seo and S. il Seok, Compositional engineering of perovskite materials for high-performance solar cells, *Nature*, 2015, **517**, 476–480.

78 F. Chen, L. Xu, Y. Li, T. Fang, T. Wang, M. Salerno, M. Prato and J. Song, Highly efficient sky-blue light-emitting diodes based on Cu-treated halide perovskite nanocrystals, *J. Mater. Chem. C*, 2020, **8**, 13445–13452.

79 C. Bi, S. Wang, Q. Li, S. V. Kershaw, J. Tian and A. L. Rogach, Thermally Stable Copper(II)-Doped Cesium Lead Halide Perovskite Quantum Dots with Strong Blue Emission, *J. Phys. Chem. Lett.*, 2019, **10**, 943–952.

80 A. De, S. Das, N. Mondal and A. Samanta, Highly Luminescent Violet- and Blue-Emitting Stable Perovskite Nanocrystals, *ACS Mater. Lett.*, 2019, **1**, 116–122.

81 Y.-C. Chen, H.-L. Chou, J.-C. Lin, Y.-C. Lee, C.-W. Pao, J.-L. Chen, C.-C. Chang, R.-Y. Chi, T.-R. Kuo, C.-W. Lu and D.-Y. Wang, Enhanced Luminescence and Stability of Cesium Lead Halide Perovskite CsPbX$_3$ Nanocrystals by Cu2+-Assisted Anion Exchange Reactions, *J. Phys. Chem. C*, 2019, **123**, 2353–2360.

82 S. G. Motti, D. Meggiolaro, S. Martani, R. Sorrentino, A. J. Barker, F. De Angelis and A. Petrozza, Defect Activity in Lead Halide Perovskites, *Adv. Mater.*, 2019, **31**, 1901183.

83 A. Mannodi-Kanakkithodi, J. Park, D. H. Cao, N. Jeon, A. B. F. Martinson and M. K. Y. Chan, First-principles Study of Intrinsic and Extrinsic Point Defects in Lead-Based Hybrid Perovskites, in *2018 IEEE 7th World Conference on Photovoltaic Energy Conversion (WCPEC) (A Joint Conference of 45th IEEE PVSC, 28th PVSEC & 34th EU PVSEC)*, 2018, pp. 495–498.

84 W. Kohn and L. J. Sham, Self-Consistent Equations Including Exchange and Correlation Effects, *Phys. Rev.*, 1965, **140**, A1133–A1138.

85 P. E. Blöchl, Projector augmented-wave method, *Phys. Rev. B: Condens. Matter Mater. Phys.*, 1994, **50**, 17953–17979.

86 J. Enkovaara, C. Rostgaard, J. J. Mortensen, J. Chen, M. Dułak, L. Ferrighi, J. Gavnholt, C. Glinsvad, V. Haikola, H. A. Hansen, H. H. Kristoffersen, M. Kuisma, A. H. Larsen, L. Lehtovaara, M. Ljungberg, O. Lopez-Acevedo, P. G. Moses, J. Ojanen, T. Olsen, V. Petzold, N. A. Romero, J. Stausholm-Møller, M. Strange, G. A. Tritsaris, M. Vanin, M. Walter, B. Hammer, H. Häkkinen, G. K. H. Madsen, R. M. Nieminen, J. K. Nørskov, M. Puska, T. T. Rantala, J. Schiøtz, K. S. Thygesen and K. W. Jacobsen, Electronic structure calculations with GPAW: a real-space implementation of the projector augmented-wave method, *J. Phys.: Condens. Matter*, 2010, **22**, 253202.

87 A. Hjorth Larsen, J. Jørgen Mortensen, J. Blomqvist, I. E. Castelli, R. Christensen, M. Dułak, J. Friis, M. N. Groves, B. Hammer, C. Hargus, E. D. Hermes, P. C. Jennings, P. Bjerre Jensen, J. Kermode, J. R. Kitchin, E. Leonhard Kolsbjerg, J. Kubal, K. Kaasbjerg, S. Lysgaard, J. Bergmann Maronsson, T. Maxson, T. Olsen, L. Pastewka, A. Peterson, C. Rostgaard, J. Schiøtz, O. Schütt, M. Strange, K. S. Thygesen, T. Vegge, L. Vilhelmsen, M. Walter, Z. Zeng and K. W. Jacobsen, The atomic simulation environment—a Python library for working with atoms, *J. Phys.: Condens. Matter*, 2017, **29**, 273002.

88 J. P. Perdew, K. Burke and M. Ernzerhof, Generalized Gradient Approximation Made Simple, *Phys. Rev. Lett.*, 1996, **77**, 3865–3868.

89 J. Buckeridge, D. O. Scanlon, A. Walsh and C. R. A. Catlow, Automated procedure to determine the thermodynamic stability of a material and the range of chemical potentials necessary for its formation relative to competing phases and compounds, *Comput. Phys. Commun.*, 2014, **185**, 330–338.

90 M. Gjerding, T. Skovhus, A. Rasmussen, F. Bertoldo, A. H. Larsen, J. J. Mortensen and K. S. Thygesen, Atomic Simulation Recipes: A Python framework and library for automated workflows, *Comput. Mater. Sci.*, 2021, **199**, 110731.

91 K. S. T. Jens Jørgen Mortensen and M. Gjerding, MyQueue: Task and workflow scheduling system, *J. Open Source Softw.*, 2020, **45**, 1844.